



Cite this: DOI: 10.1039/c5cy02005k

Received 24th November 2015,  
Accepted 5th January 2016

DOI: 10.1039/c5cy02005k

www.rsc.org/catalysis

## Phenylacetylene hydrogenation on Au@Ni bimetallic core-shell nanoparticles synthesized under mild conditions†

A. B. Vysakh,<sup>ab</sup> Anish Lazar,<sup>ab</sup> V. Yadukiran,<sup>a</sup> A. P. Singh<sup>a</sup> and C. P. Vinod<sup>\*abc</sup>

The synthesis of Au@Ni bimetallic core-shell nanoparticles through an energy efficient (lower temperature) route in oleylamine following a sequential reduction strategy is reported. The method is found to be useful for the synthesis of a very thin nickel shell (2 nm) over a gold core (15 nm). Synergistic effects are observed in catalyzing phenylacetylene hydrogenation under different solvent conditions.

Metals and metal oxides have been widely used in their “nano” form for diverse physical, biological and chemical applications.<sup>1–3</sup> Nanocatalysis is a rapidly growing field in heterogeneous catalysis which involves the use of metal/metal oxide nanoparticles for tailoring the catalytic activity and selectivity towards the optimum.<sup>4–8</sup> In the case of metal nanoparticles, the quantum size effects are found to have profound effects in their physical and chemical properties compared to bulk materials.<sup>9,10</sup> Vast improvements in the characterization tools have led to a better understanding of the atomic details of the materials, especially catalytic materials, which has led to rapid developments in tailor-made heterogeneous catalyst design.<sup>11–13</sup> In this regard, designing catalysts through surface modification *via* a bimetallic route has shown a lot of promise.<sup>14–16</sup> Bimetallic nanoparticles, especially in the form of core-shell morphology, can be considered as a model system where the role of core material, shell thickness, and interface<sup>17–19</sup> can be fine tuned for desired applications. This core-shell morphology also extends the possibility of tuning various properties especially catalytic activity and selectivity by controlling their chemical

composition and relative sizes of the core and shell.<sup>20,21</sup> Here, instead of supported catalysts, colloidal nanoparticles function as a true model, and they bridge the properties of homogeneous catalysis and heterogeneous catalysis.<sup>22</sup> The catalytic efficiency is largely governed by the Sabatier principle, whereby the interactions of adsorbate molecules are largely controlled by the electronic structure of the catalyst surface.<sup>23</sup> The combination of metals like gold (Au) and nickel (Ni) has been less explored due to their large lattice mismatch but are the ones which can demonstrate fascinating catalytic properties.<sup>24</sup> Gold nanoparticles are widely known for oxidation reactions,<sup>25–27</sup> whereas nickel acts as a good hydrogenation catalyst.<sup>28</sup> In this report, we show that Au@Ni core-shell nanoparticles can be synthesized at a relatively milder temperature than the ones reported previously.<sup>29,30</sup> Further, they are shown to synergistically catalyze phenylacetylene (PA) hydrogenation reaction to styrene which is an industrially important commodity for polymer synthesis. It should be noted that a commercially more viable process for the production of styrene is through the dehydrogenation route of ethylbenzene (EB).<sup>31</sup> The importance of finding an optimum catalyst for PA hydrogenation stems from the fact that any trace amount of PA in the styrene feedstock is found to adversely affect the polystyrene product distribution.<sup>32</sup>

The synthesis of a Au core nanoparticle and the growth of Ni as a shell over the core can be monitored by the UV-vis spectroscopy technique. The wine red colour of the colloidal solution after reduction of gold ions due to the surface plasmon resonance (SPR) indicates the formation of gold (Au) nanoparticles.<sup>33</sup> The surface plasmon resonance appears as a band in the UV-vis spectrum. Here, the preformed gold seeds act as nucleation sites for the adsorption of the nickel ions in the second stage which subsequently undergo reduction upon addition of a hydrazine/NaOH mixture at 80 °C to form the bimetallic nanoparticles (see the ESI† for the synthesis procedure). The previous literature analysis on the synthesis of Au–Ni or Ni nanoparticles using oleylamine as the solvent shows that the reduction of Ni ions take place above

<sup>a</sup> Catalysis Division, CSIR-National Chemical Laboratory, Dr. Homi Bhabha Road, Pune, India. E-mail: cp.vinod@ncl.res.in; Fax: +91 20 25902633; Tel: +91 20 25902086

<sup>b</sup> Academy of Scientific and Innovative Research (AcSIR), Anusandhan Bhawan, 2 Rafi Marg, New Delhi, Delhi 110001, India

<sup>c</sup> Center of Excellence on Surface Science, CSIR-National Chemical Laboratory, Pune, India

† Electronic supplementary information (ESI) available. See DOI: 10.1039/c5cy02005k

200 °C resulting in the formation of Ni nanoparticles.<sup>34,35</sup> Here, we are able to bring down the reduction temperature below 100 °C with the successful generation of Au@Ni bimetallic nanoparticles. The complete damping of the gold plasmon band in the later stage of nickel reduction shows the successive formation of the nickel shell over the gold core. The UV-vis spectra obtained at different stages of the synthesis are shown in Fig. S1†. Curve a in the UV-vis spectra indicates the first stage of gold reduction which shows plasmon absorbance around 515 nm. Curve b in Fig. S1† corresponds to the final stage of nickel reduction over the gold nanoparticles which confirms the complete damping of gold plasmon.<sup>20</sup> Powder XRD analysis of Au@Ni bimetallic nanostructures are shown in Fig. S2†. The diffraction from the gold and nickel planes indicates that both metals exist in the FCC lattice without any alloying effects. The fairly large FWHM (full width at half maximum) values of the XRD peaks indicate the small size of the nanoparticles. The particle size analysis using the Scherrer equation corroborated with the TEM analysis and confirms the total size of Au@Ni core-shell nanoparticles to be around 20 nm in average. The diffractions in Fig. S2† correspond to gold alone (curve b), nickel alone (curve a) and Au@Ni (curve c) core-shell nanoparticles. The diffractions at  $2\theta$  values of 38.2, 44.3 and 64.6 correspond to Au(111), Au(200) and Au(220), respectively.<sup>36</sup> Similarly, Ni(111), Ni(200) and Ni(220) are diffracted at  $2\theta$  values of 44.5, 51.8 and 76.4, respectively.<sup>34</sup> Since there are strong overlap of diffractions from Au(200) and Ni(111), the most discernable peak for the identification of Ni is at a  $2\theta$  value of 51.8. The less intense and very broad peak at 51.8 in the enlarged Fig. S2(II)† (shaded region) of the Au@Ni core-shell nanoparticle gives a clear confirmation of the thin nickel lattice on the Au core. It is understandable that the diffractions from the nickel lattice in the case of Au@Ni are not clearly visible because of the extremely thin nickel shell on the gold surface. However, in the case of nickel nanoparticles alone, the reflections are clearly visible and they confirm the formation of a pure FCC phase of the nickel metal.<sup>34</sup> Fig. 1 shows the TEM image of the as-synthesized bimetallic Au@Ni nanostructures drop cast on the Cu grid after sonication for 5

minutes. HR-TEM analysis of Au@Ni bimetallic nanoparticles confirmed the core-shell morphology of nanoparticles through lattice fringe analysis and contrast difference between a heavier noble metal (Au) and a lighter non-noble (Ni) metal. The large area TEM analysis (Fig. 1a and S3, ESI†) showed the size distribution of nanoparticles (~20 nm), and EDX (energy dispersive X-ray) analysis (Fig. 1e) indicated the elemental composition between both metals. From Fig. 1b and c, it is evident that the overall size of the core-shell nanoparticle is on average around 20 nm with a core size of around 15 nm and a shell thickness of approximately 2 nm. The HR-TEM image of a single particle in Fig. 1b shows a clear contrast difference between the two metals in an isolated particle indicating the formation of a core-shell morphology.<sup>37</sup> The lattice fringe analysis at the core and the shell (Fig. 1d) gave values of 2.38 Å and 2.04 Å, respectively, confirming that Ni is present as the shell and Au as the core.<sup>35</sup> The FFT (fast Fourier transform) pattern (inset of Fig. 1d) also indicated the presence of gold and nickel  $d$ -spacing values. Despite the large lattice mismatch between the Au and Ni systems, there have been recent reports that it is indeed possible to epitaxially grow Ni on Au.<sup>38</sup> Fig. 1c shows moiré fringes which arise due to the mismatch of lattice parameters of gold and nickel.<sup>38</sup> The moiré fringe values (1.5 nm) were found to be in agreement with the literature values for gold and nickel.<sup>35</sup> Thus, the microscopy observations provided here gave clear evidence for the formation of a Au@Ni core-shell system under milder conditions reported so far with oleylamine as the solvent and reducing agent.<sup>39</sup> The EDX analysis (Fig. 1e) showed the elemental composition of approximately 1:0.25 (see Fig. S3† for quantification results) for gold to nickel which is in good agreement with the metal precursor ratios used for the synthesis. Our previous report demonstrated the need for an extremely thin nickel shell for the demonstration of synergistic effects in catalysis.<sup>21</sup> To understand the electronic state of the metals especially at the surface, we carried out an XPS study by drop casting the sample on a silicon wafer. Fig. S4† shows the wide area scan of the as-synthesized samples. It shows the presence of characteristic signature peaks from gold, nickel, oxygen and carbon. The peak positions were calibrated by considering a carbon standard value at 284.6 eV. Fig. 2a and b are the individual scans performed for gold and nickel core levels, respectively. The Ni  $2p_{3/2}$  spectra (Fig. 2b) from the bimetallic Au@Ni core-shell provide evidence for the metallic feature (852.6 eV) along with hydroxide features at 855.8 eV.<sup>29</sup> The solution phase synthesis of nickel nanoparticles always produces some amount of hydroxides on the surface which is unavoidable under such synthesis conditions. It must be noted that even though all the syntheses were carried out in ambient atmosphere with samples dried in the open atmosphere, the material managed to prevent the complete aerial oxidation of nickel nanoparticles. The absence of a NiO peak at 854 eV in the nickel spectra and the presence of more than 50% of metallic nickel species even after exposure to the atmosphere proved the strong surface

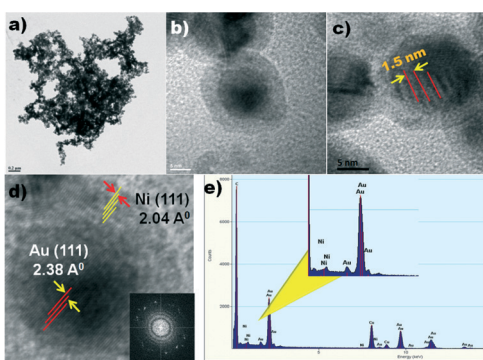


Fig. 1 (a) TEM, (b–d) HR-TEM images and (e) EDX data of Au@Ni core-shell nanoparticles. The inset of (d) shows the FFT pattern of an individual Au@Ni nanoparticle.

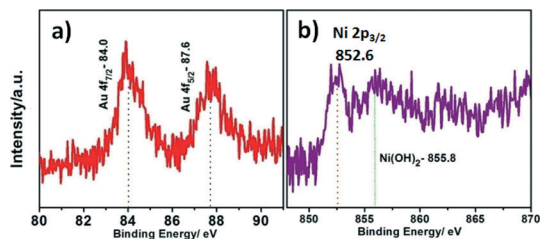


Fig. 2 XPS core-level spectra of Au 4f (a) and Ni 2p (b) obtained for Au@Ni core-shell nanoparticles. The violet dotted line in (b) indicates the nickel metallic feature, whereas green corresponds to the hydroxide feature.

modification in the Au–Ni bimetallic combination. This observation is a direct demonstration of the gold core-induced surface modification of the ultrathin nickel nanoshell which shows resistance towards surface oxidation.<sup>40</sup> These types of bimetallic systems which are geometrically and electronically modified due to the core–shell morphology are well known in the literature for enhanced physical and chemical properties including good catalytic performances.<sup>19,41</sup> The individual gold scan in XPS (Fig. 2a) showed binding energy values of 84 eV ( $4f_{7/2}$ ) and 87.6 eV ( $4f_{5/2}$ ) which are typical of metallic gold. These two peaks arise due to the spin orbit splitting of 4f energy levels and the ejection of 4f core level photoelectrons. The values obtained for the Au(4f) core level also prove the absence of any unreduced Au(3+) in the final catalyst.<sup>42</sup> Nickel (in a face-centred cubic structure) is well known for its ferromagnetic behaviour, and we explored the magnetic properties of these Au@Ni core-shell nanoparticles by measuring the hysteresis loop using SQUID. In Fig. S5,<sup>†</sup> we show the magnetic behaviour of Au@Ni core-shell nanoparticles which demonstrate typical hysteric behaviour of a ferromagnetic Ni (ref. 34) with a very low saturation magnetization of 2 emu  $\text{gm}^{-1}$  in an applied field of 6 kOe. The inset of the image (Fig. S5, ESI<sup>†</sup>) shows the remanent magnetisation of the material along with very low coercivity values. The synthesized core-shell nanomaterials were tested for potential applications in catalysis by carrying out hydrogenation reactions. The first row transition elements are prone to oxidation, even under ambient conditions as they are known to form surface oxides which poison the catalytic activity of the materials. The formation of oxide layers<sup>43</sup> is found to limit the hydrogenation pathway; hence, the need of retaining of the metallic feature is necessary for efficient catalytic activity. Our previous reports showed that synergistic effects are observed in core–shell bimetallic combinations up to around 2 nm shell thickness compared to the individual monometallic counterparts.<sup>21</sup> To test the efficiency of the synthesized Au@Ni bimetallic system, we checked the catalytic activity of core–shell particles for phenylacetylene (PA) hydrogenation reaction. This is an industrially important reaction where the partially hydrogenated product styrene is an important starting material for many industrially relevant polymers.<sup>32</sup> In addition, the reaction is a testing ground for activity and selectivity correlations where ethylbenzene is also a widely reported

hydrogenation product of phenylacetylene.<sup>44</sup> The reaction was carried out using a stirred type Parr reactor which can go up to 300 °C in temperature and up to 50 bar pressure. We optimized the reaction conditions by carrying out a range of experiments by varying the pressure and temperature conditions (conditions shown in the figure caption). The reactions were carried out in different solvents like methanol, tetrahydrofuran (THF) and dichloromethane (DCM). These solvents were chosen as it was previously reported that the selectivity towards the desired product (styrene) crucially depends on the solvent.<sup>28</sup> The reaction mixture was analyzed with the help of an offline GC. Initially, we tested the core–shell systems with their monometallic counterparts for understanding the enhancement in catalytic activity. To exclude the influence of quantum size effects in catalytic activity, we compared the activity of bare Au and Ni nanoparticles having a similar size (around 15 and 20 nm, respectively) with Au@Ni core-shell nanoparticles. Fig. 3 shows the phenylacetylene (PA) hydrogenation for Au nanoparticles, Ni nanoparticles and Au@Ni core-shell nanoparticles in methanol (MeOH)

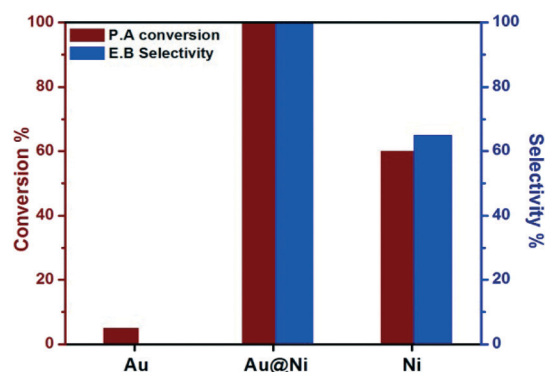


Fig. 3 Phenylacetylene conversion (brown) and ethylbenzene selectivity (blue) in methanol solvent obtained for Au@Ni core-shell catalysts and their monometallic counterparts (gold and nickel). The reaction conditions are given as follows: 50 °C and 50 psi  $\text{H}_2$  pressure [catalyst weight – 5 mg, substrate – 5 mmol and reaction time – 4 hours].

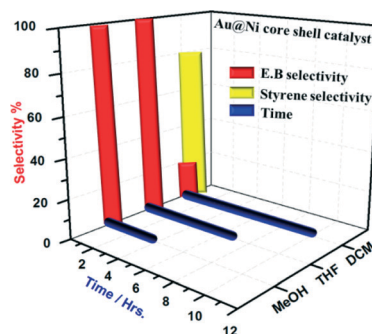


Fig. 4 Selectivity (red and yellow) obtained for complete conversion of PA in various solvents by using Au@Ni core-shell catalysts. The blue bar represents the time taken for complete conversion [reaction conditions: for MeOH and THF: 50 °C and 50 psi  $\text{H}_2$  pressure; catalyst – 5 mg; substrate – 5 mmol. For DCM: 40 °C and 50 psi  $\text{H}_2$  pressure; catalyst – 10 mg; substrate – 1 mmol].

**Table 1** Hydrogenation results obtained for PA by using Au@Ni catalysts and Ni nanoparticles in MeOH (50 ml) and DCM (50 ml) under various temperatures [in MeOH and DCM, the substrate is 5 and 1 mmol, respectively]

Serial no.	Catalyst	Amount (mg)	Time (h)	Solvent	Temp. (°C)	Press. (psi)	Conversion	Selectivity (%) EB/styrene
1	Ni alone	5	4	MeOH	50	50	60%	65/35
2	Au@Ni	5	4	MeOH	50	50	100%	100/0
3	Ni alone	5	4	MeOH	30	50	35%	50/50
4	Au@Ni	5	4	MeOH	30	50	60%	60/40
5	Ni alone	10	10	DCM	40	50	55%	25/75
6	Au@Ni	10	10	DCM	40	50	100%	20/80
7	Ni alone	10	10	DCM	30	50	30%	20/80
8	Au@Ni	10	10	DCM	30	50	65%	15/85

solvent carried out at 50 °C and 50 psi pressure. From the reactivity analysis in Fig. 3, it can be seen that Au@Ni core-shell nanoparticles showed excellent reactivity and selectivity for ethylbenzene (EB). Under similar conditions, we could achieve only 60% conversion and 65% selectivity to EB on Ni nanoparticles with Au nanoparticles being negligibly active. The poor activity on gold can be attributed to the large size of Au nanoparticles in our case (~15 nm), while a recent report has suggested the particle size of ~5 nm for Au nanoparticles to be optimum for selective conversion towards styrene.<sup>45</sup> In the case of Ni nanoparticles, most of the phenylacetylene hydrogenation has been carried out using intermetallics of nickel to tune the selectivity towards styrene.<sup>46–48</sup> The activity of Au@Ni nanoparticles reported here shows that the catalyst is extremely active where the triple bond in PA can be totally saturated under moderate conditions.

The effect of solvent on PA hydrogenation is shown in Fig. 4 and Table 1, respectively. The reaction results show that there is a strong dependence of solvent and temperature on the conversion rates. We found that using methanol and THF as solvent, the optimum conditions for hydrogenation of carbon-carbon triple bonds are 50 °C and 50 psi pressure with 5 mg of the catalysts with 100% conversion and selectivity towards ethylbenzene. We observed that the rate was lower in THF which took almost 7 hours for complete conversion compared to 4 hours in methanol. In DCM solvent also, we achieved similar conversions, whereas the hydrogenation results obtained for phenylacetylene in dichloromethane as solvent showed 80% selectivity towards styrene (Fig. 4; see also Fig. S6, ESI† for GC results), which has a high commercial value in the polymer industry, and the remaining product was ethylbenzene. The effect of solvent plays a crucial role in deciding the selectivity which is known for some other bimetallic combination like Fe-Ni reported by Polshettiwar *et al.*<sup>28</sup> We found that our catalyst is highly active under these mild reaction conditions of temperature and pressure. In DCM solvent, the rate was much slower because of the lower temperature (40 °C) used for the hydrogenation reaction. We could not go beyond 40 °C as DCM starts to boil beyond that temperature. For complete conversion in DCM solvent, it took 10 hours but with good selectivity towards styrene. Under similar conditions, nickel nanoparticles showed only 55% conversion demonstrating the synergistic effects in Au@Ni core-

shell nanoparticles. From the conversion and selectivity analysis, we found that methanol is more suitable for ethylbenzene production *via* the complete hydrogenation and DCM is suitable for the partial hydrogenation to styrene. To explore further on the temperature and solvent effects, we carried out a series of hydrogenation reactions and the results are tabulated in Table 1. A decrease in temperature from 50 °C to room temperature (30 °C) marked a decrease of ~40% in the conversion rates of both solvents (MeOH and DCM). Interestingly, the selectivity towards styrene is higher while lowering the temperature which shows that the complete hydrogenation pathway goes through styrene. From these results, we can conclude that the selectivity and rate towards a desired product can be controlled by temperature and solvent.

In conclusion, we report here a facile energy efficient route for the synthesis of highly lattice mismatched gold-nickel core-shell bimetallic nanoparticles. The nickel shell thickness over the gold core is fine tuned to obtain maximum catalytic efficiency of the Au@Ni core-shell catalysts. The bare nanoparticles without any support showed good catalytic enhancement towards hydrogenation of PA with high selectivity towards styrene or ethylbenzene with respect to the solvent and temperature. The catalysts were found to show the activity under mild conditions of temperature and pressure.

## Acknowledgements

CPV thanks Dr. C. S. Gopinath for constant support and encouragement. The authors thank Dr. P. A. Joy and Govind K. Raj for magnetic measurements. ABV thanks UGC for the research fellowship. This work was supported by CSIR through the project CSC0404 (CoE on Surface Science) for CPV.

## References

- 1 A. Kudo and Y. Miseki, *Chem. Soc. Rev.*, 2009, **38**, 253–278.
- 2 L. H. Reddy, J. L. Arias, J. Nicolas and P. Couvreur, *Chem. Rev.*, 2012, **112**, 5818–5878.
- 3 L. L. Chng, N. Erathodiyil and J. Y. Ying, *Acc. Chem. Res.*, 2013, **46**, 1825–1837.
- 4 Z.-C. Zhang, B. Xu and X. Wang, *Chem. Soc. Rev.*, 2014, **43**, 7870–7886.
- 5 B. F. Johnson, *Top. Catal.*, 2003, **24**, 147–159.

- 6 D. Astruc, F. Lu and J. R. Aranzaes, *Angew. Chem., Int. Ed.*, 2005, **44**, 7852–7872.
- 7 M.-C. Daniel and D. Astruc, *Chem. Rev.*, 2003, **104**, 293–346.
- 8 P. Herves, M. Perez-Lorenzo, L. M. Liz-Marzan, J. Dzubielia, Y. Lu and M. Ballauff, *Chem. Soc. Rev.*, 2012, **41**, 5577–5587.
- 9 S. Eustis and M. A. El-Sayed, *Chem. Soc. Rev.*, 2006, **35**, 209–217.
- 10 C. P. Vinod, G. U. Kulkarni and C. N. R. Rao, *Chem. Phys. Lett.*, 1998, **289**, 329–333.
- 11 J. C. Yang, M. W. Small, R. V. Grieshaber and R. G. Nuzzo, *Chem. Soc. Rev.*, 2012, **41**, 8179–8194.
- 12 C. P. Vinod, *Catal. Today*, 2010, **154**, 113–117.
- 13 C. P. Vinod, *New and Future Developments in Catalysis: Catalysis by Nanoparticles*, Elsevier, 2013, ch. 12, pp. 289–304.
- 14 H.-L. Jiang and Q. Xu, *J. Mater. Chem.*, 2011, **21**, 13705–13725.
- 15 M. Sankar, N. Dimitratos, P. J. Miedziak, P. P. Wells, C. J. Kiely and G. J. Hutchings, *Chem. Soc. Rev.*, 2012, **41**, 8099–8139.
- 16 F. Tao, *Chem. Soc. Rev.*, 2012, **41**, 7977–7979.
- 17 J. Wu, P. Li, Y.-T. Pan, S. Warren, X. Yin and H. Yang, *Chem. Soc. Rev.*, 2012, **41**, 8066–8074.
- 18 S. Alayoglu, A. U. Nilekar, M. Mavrikakis and B. Eichhorn, *Nat. Mater.*, 2008, **7**, 333–338.
- 19 P. Strasser, S. Koh, T. Anniyev, J. Greeley, K. More, C. Yu, Z. Liu, S. Kaya, D. Nordlund, H. Ogasawara, M. F. Toney and A. Nilsson, *Nat. Chem.*, 2010, **2**, 454–460.
- 20 A. M. Henning, J. Watt, P. J. Miedziak, S. Cheong, M. Santonastaso, M. Song, Y. Takeda, A. I. Kirkland, S. H. Taylor and R. D. Tilley, *Angew. Chem., Int. Ed.*, 2013, **52**, 1477–1480.
- 21 A. B. Vysakh, C. L. Babu and C. P. Vinod, *J. Phys. Chem. C*, 2015, **119**, 8138–8146.
- 22 S. Schaueremann, N. Nilius, S. Shaikhutdinov and H. J. Freund, *Acc. Chem. Res.*, 2013, **46**, 1673–1681.
- 23 J. K. Norskov, T. Bligaard, J. Rossmeisl and C. H. Christensen, *Nat. Chem.*, 2009, **1**, 37–46.
- 24 X. W. Zhou and H. N. G. Wadley, *Philos. Mag.*, 2004, **84**, 193–212.
- 25 T. V. Choudhary and D. W. Goodman, *Top. Catal.*, 2002, **21**, 25–34.
- 26 B. K. Min and C. M. Friend, *Chem. Rev.*, 2007, **107**, 2709–2724.
- 27 B. E. Nieuwenhuys, A. C. Gluhoi, E. D. L. Rienks, C. J. Weststrate and C. P. Vinod, *Catal. Today*, 2005, **100**, 49–54.
- 28 V. Polshettiwar, B. Baruwati and R. S. Varma, *Green Chem.*, 2009, **11**, 127–131.
- 29 H. Zhang, J. Ding, G. Chow, M. Ran and J. Yi, *Chem. Mater.*, 2009, **21**, 5222–5228.
- 30 V. A. Bharathan, G. K. Raj, P. A. Joy and C. P. Vinod, *Part. Part. Syst. Charact.*, 2014, **31**, 236–244.
- 31 A. K. Venugopal, A. T. Venugopalan, P. Kaliyappan and T. Raja, *Green Chem.*, 2013, **15**, 3259–3267.
- 32 D. B. Priddy and J. M. Roe, *US Pat. No. 4,389,517*, 1983.
- 33 P. Lakshminarayana and X. Qing-Hua, *Nanotechnology*, 2009, **20**, 185606.
- 34 Y. Chen, D.-L. Peng, D. Lin and X. Luo, *Nanotechnology*, 2007, **18**, 505703.
- 35 H. She, Y. Chen, X. Chen, K. Zhang, Z. Wang and D.-L. Peng, *J. Mater. Chem.*, 2012, **22**, 2757–2765.
- 36 M. Aslam, L. Fu, M. Su, K. Vijayamohanan and V. P. Dravid, *J. Mater. Chem.*, 2004, **14**, 1795–1797.
- 37 D. Wang and Y. Li, *J. Am. Chem. Soc.*, 2010, **132**, 6280–6281.
- 38 M. Tsuji, D. Yamaguchi, M. Matsunaga and K. Ikeda, *Cryst. Growth Des.*, 2011, **11**, 1995–2005.
- 39 S. Carenco, C. Boissière, L. Nicole, C. Sanchez, P. Le Floch and N. Mézailles, *Chem. Mater.*, 2010, **22**, 1340–1349.
- 40 G. U. Kulkarni and C. P. Vinod, *Appl. Surf. Sci.*, 1997, **115**, 336–341.
- 41 A. U. Nilekar, S. Alayoglu, B. Eichhorn and M. Mavrikakis, *J. Am. Chem. Soc.*, 2010, **132**, 7418–7428.
- 42 H. Zhang, B. Dai, W. Li, X. Wang, J. Zhang, M. Zhu and J. Gu, *J. Catal.*, 2014, **316**, 141–148.
- 43 S. Sarkar, A. K. Sinha, M. Pradhan, M. Basu, Y. Negishi and T. Pal, *J. Phys. Chem. C*, 2010, **115**, 1659–1673.
- 44 R. V. Chaudhari, R. Jaganathan, D. S. Kolhe, G. Emig and H. Hofmann, *Chem. Eng. Sci.*, 1986, **41**, 3073–3081.
- 45 L. Shao, X. Huang, D. Teschner and W. Zhang, *ACS Catal.*, 2014, **4**, 2369–2373.
- 46 X. Chen, A. Zhao, Z. Shao, C. Li, C. T. Williams and C. Liang, *J. Phys. Chem. C*, 2010, **114**, 16525–16533.
- 47 X. Chen, M. Li, J. Guan, X. Wang, C. T. Williams and C. Liang, *Ind. Eng. Chem. Res.*, 2012, **51**, 3604–3611.
- 48 C. Li, Y. Chen, S. Zhang, J. Zhou, F. Wang, S. He, M. Wei, D. G. Evans and X. Duan, *ChemCatChem*, 2014, **6**, 824–831.